

Possible Population III Remnants at Redshift 3.5

Neil H. M. Crighton,^{1*} John M. O’Meara² and Michael T. Murphy¹

¹*Centre for Astrophysics and Supercomputing, Swinburne University of Technology, Hawthorn, Victoria 3122, Australia*

²*Department of Chemistry & Physics, Saint Michael’s College, One Winooski Park, Colchester VT, 05439*

To appear in MNRAS letters

ABSTRACT

The first stars, known as Population III (PopIII), produced the first heavy elements, thereby enriching their surrounding pristine gas. Previous detections of metals in intergalactic gas clouds, however, find a heavy element enrichment larger than 1/1000 times that of the solar environment, higher than expected for PopIII remnants. In this letter we report the discovery of a Lyman limit system (LLS) at $z = 3.53$ with the lowest metallicity seen in gas with discernable metals, $10^{-3.41 \pm 0.26}$ times the solar value, at a level expected for PopIII remnants. We make the first relative abundance measurement in such low metallicity gas: the carbon-to-silicon ratio is $10^{-0.26 \pm 0.17}$ times the solar value. This is consistent with models of gas enrichment by a PopIII star formation event early in the Universe, but also consistent with later, Population II enrichment. The metals in all three components comprising the LLS, which has a velocity width of 400 km s^{-1} , are offset in velocity by $\sim +6 \text{ km s}^{-1}$ from the bulk of the hydrogen, suggesting the LLS was enriched by a single event. Relative abundance measurements in this near-pristine regime open a new avenue for testing models of early gas enrichment and metal mixing.

Key words: dark ages, reionization, first stars – quasars: absorption lines – galaxies: abundances – intergalactic medium

1 INTRODUCTION

In the first three minutes after the Big Bang, nucleosynthesis determined the hydrogen-to-helium ratio of pristine gas, which contained no elements heavier than beryllium. The first heavier elements (‘metals’) were manufactured by PopIII stars, and their explosions polluted this pristine gas with metals (Yoshida et al. 2004; Ciardi & Ferrara 2005). The amount of pristine gas polluted and the relative abundances of different heavy elements encodes information about the mass distribution, nucleosynthetic processes and other characteristics of the first stars (Heger & Woosley 2010; Bromm 2013). The recent discovery of gas without any observable metals, two billion years after the big bang (Fumagalli et al. 2011), has opened the possibility of finding new clouds enriched to the levels expected for PopIII remnants. However, despite targeted searches (e.g. Cooke et al. 2011) for metal-poor systems, all gas clouds where metals have been detected are found to be enriched to at least 1/1000 the solar value, higher than expected for gas enriched by the first stars.

Here we report the discovery of a gas cloud with metallicity $\sim 1/2500$ solar, found by searching through archived

observations of quasars made using the UVES echelle spectrograph on the ESO Very Large Telescope.

2 DATA

The cloud is part of an absorption system towards the background quasar SDSS J124957.23–015928.8 ($z_{\text{em}} = 3.634$, Schneider et al. 2003). We identified the system by its optically thick H I absorption at the Lyman limit ($\lambda_{\text{rest}} = 912 \text{ \AA}$), which attenuates the quasar continuum at observed wavelengths shorter than 4140 \AA (Fig. 1). This Lyman limit system (LLS), henceforth LLS1249, has a redshift $z = 3.53$, corresponding to 1.8 billion years after the big bang (assuming a cosmology found by the Planck Collaboration, 2015).

The archived UVES spectra of SDSS J124957.23–015928.8 were taken for program 075.A–0464 (P.I. Kim), and cover a wavelength range $3750\text{--}6800 \text{ \AA}$ at a resolution of 6 km s^{-1} full width at half maximum (FWHM). Our analysis also uses an archived HIRES spectrum ($4110\text{--}8675 \text{ \AA}$, FWHM 6 km s^{-1}) of the quasar taken at the Keck telescope during program U157Hb (P.I. Prochaska), and a Sloan Digital Sky Survey (SDSS) spectrum with FWHM $\sim 150 \text{ km s}^{-1}$.

The UVES spectra were reduced using the UVES pipeline, and combined using the UVES_POPLER code. A detailed explanation of the reduction procedure is provided by,

* E-mail: neilcrighton@gmail.com

Table 1. The redshifts, column densities, and b values for the three H I components. The $N_{\text{H I}}$ errors include a contribution from uncertainties in placing the continuum (see the right panel of Fig. 1).

Comp.	z	δv (km s $^{-1}$)	$\log(N_{\text{H I}}/\text{cm}^{-2})$	b (km s $^{-1}$)
1	3.524038 (04)	-400	17.15 ± 0.04	18.9 ± 0.3
2	3.525285 (12)	-317	17.20 ± 0.03	19.2 ± 0.9
3	3.530073 (04)	0	17.33 ± 0.03	20.9 ± 0.3

for example, Bagdonaite et al. (2012). The HIRES spectrum was reduced using the HIRESREDUX code as described by O’Meara et al. (2015). For all spectra we estimated the continuum over the Ly α forest using a smoothly varying spline function, fitted by eye with interactive tools.

3 ANALYSIS

The Lyman series in the UVES combined spectrum reveals three H I absorption components spanning 400 km s $^{-1}$ (Fig. 1). The ratio between the residual flux and the continuum at the Lyman limit sets the total H I column density, $N_{\text{H I}}$, for these components, and their Lyman series determine how $N_{\text{H I}}$ is shared among them. We fit Voigt profiles to the three components to find their linewidths, redshifts and $N_{\text{H I}}$. Table 1 lists the best-fitting H I parameters, and Fig. 2 shows the Lyman series transitions which best constrain $N_{\text{H I}}$ for the highest redshift component, component 3. We checked our H I model by comparing it to the SDSS spectrum, and find that it provides a good match to the partial Lyman limit and the Lyman series in the lower resolution spectrum.

The strongest metal transitions detectable for LLSs, which are invariably highly ionized, are those of single, double and triple-ionized carbon and silicon (C II 1334, C III 977, C IV 1548/1550 and Si II 1260, Si III 1206, Si IV 1393/1402). C III is detected in all three components, but only component 3 has multiple metal transitions detected, so it affords the tightest constraint on the ionization state and thus the gas metallicity.

Fig. 3 shows the metal transitions in component 3, and Table 2 lists the inferred column densities and b parameters, for line detections. The line widths of the silicon and carbon transitions are each consistent with a single value, suggesting that both the low (Si III, C III) and high ionization (Si IV, C IV) transitions are produced by the same gas phase. Previous work (Prochaska & Bures 1999; D’Odorico & Petitjean 2001; Lehner et al. 2014) has shown that LLSs can be successfully modelled as gas clouds in photoionization equilibrium with an ambient UV radiation field produced by the integrated emission from galaxies and quasars (e.g. Haardt & Madau 2012, HM12). In this context, the ionization state of a cloud is determined by the ionization parameter U , the ratio of the ionizing photon density to the gas density. Assuming the gas is in photoionization equilibrium, the ratio $N_{\text{Si III}}/N_{\text{Si IV}}$ sets a lower limit $U > 10^{-3}$.¹ This corresponds to a gas volume density $n_{\text{H}} < 10^{-2}$ and H neutral fraction $x_{\text{H}} < 0.04$. The thickness of the cloud is given

¹ We note that this validates Fumagalli et al.’s (2011) assumption that $U > 10^{-3}$ in very low metallicity LLS.

Table 2. Parameters inferred for metals in the three components. Column densities are measured using the apparent optical depth method; Voigt profile fitting gives a consistent result. Upper limits are 3σ and assume an optically thin transition. Uncertainties include a 5% systematic uncertainty in the continuum level (10% inside the Ly α forest), and an uncertainty in the zero level of $0.5\sigma_{\text{flux}}$.

		Upper limits					
		Comp. 1		Comp. 2		Comp. 3	
Ion	$\log(N/\text{cm}^{-2})$	Ion	$\log(N/\text{cm}^{-2})$	Ion	$\log(N/\text{cm}^{-2})$	Ion	$\log(N/\text{cm}^{-2})$
Al II	< 10.94	Al II	< 11.31	Al II	< 11.31		
Al III	< 11.81	Al III	< 12.10	Al III	< 12.10		
C II	< 11.65	C II	< 12.42	C II	< 12.42		
N V	< 12.47	C IV	< 12.64	N V	< 12.89		
O I	< 12.08	N V	< 12.89	O I	< 12.44		
O VI	< 12.84	O I	< 12.44	O VI	< 13.17		
Fe III	< 12.07	O VI	< 13.17	Fe III	< 12.74		
Si II	< 10.50	Fe III	< 12.74				
Si IV	< 11.05	Si II	< 11.25				
		Si III	< 12.26				
		Si IV	< 12.30				

		Detections			
Comp.	Ion	$\log(N/\text{cm}^{-2})$	b (km s $^{-1}$)	z	
1	C III	$12.52^{+0.13}_{-0.13}$	10.0 ± 0.5	3.524168(06)	
1	C IV	$12.44^{+0.13}_{-0.13}$	12.0 ± 4.7	3.524168 ^b	
2	C III	$12.14^{+0.25}_{-0.18}$	9.1 ± 1.1	3.525391(10)	
3	Si II	$10.96^{+0.28}_{-0.33}$	5.4 ^c	3.530247 ^c	
3	Si III	$12.20^{+0.15}_{-0.15}$	5.4 ± 0.3	3.530247(02)	
3	Si IV	$12.04^{+0.13}_{-0.15}$	5.6 ± 0.6	3.530217(05)	
3	C III	$13.17^{+0.05}_{-0.04}$	7.7 ± 0.4	3.530222(04)	
3	C IV ^a	$12.45^{+0.08}_{-0.08}$	9.0 ± 2.2	3.530222 ^b	

^a C IV 1548 is partly blended with sky emission.

^b Fixed at the C III redshift.

^c Fixed at at Si III redshift and b .

by $N_{\text{H I}}/(x_{\text{H}}n_{\text{H}})$. We can estimate an upper limit to the cloud size from the observed width of the H I line for component 3, which has $b = 20.9 \pm 0.3$ km s $^{-1}$ (corresponding to a full width at half maximum, FWHM ~ 35 km s $^{-1}$). If the cloud is large enough it will expand with the cosmological Hubble flow, producing a velocity gradient which will be detectable in the absorption profile (Simcoe et al. 2002; Levshakov et al. 2003). The resulting line broadening is given by the Hubble parameter $H(z = 3.53) = 375$ km s $^{-1}$ Mpc $^{-1}$, and thus the largest size allowed by the broadening observed is approximately $\text{FWHM}/(375 \text{ km s}^{-1} \text{ Mpc}^{-1}) = 90$ physical kpc. This translates to an upper limit $U < 10^{-2}$, where we have included a factor of 2.2 uncertainty in the normalization of the incident radiation field in converting between the cloud volume density and the U value (e.g. Becker & Bolton 2013). The metallicity range corresponding to these U limits is $10^{-4} < Z/Z_{\odot} < 10^{-2.6}$, where we assume $\log_{10}(Z/Z_{\odot}) = [\text{Si}/\text{H}]$. If we assume a larger uncertainty in the radiation field normalization, this translates to a lower limiting metallicity.

To refine this metallicity measurement and determine other physical properties of the cloud, we use Markov Chain Monte Carlo sampling to compare the observed column densities to a grid of photoionization models, including a vari-

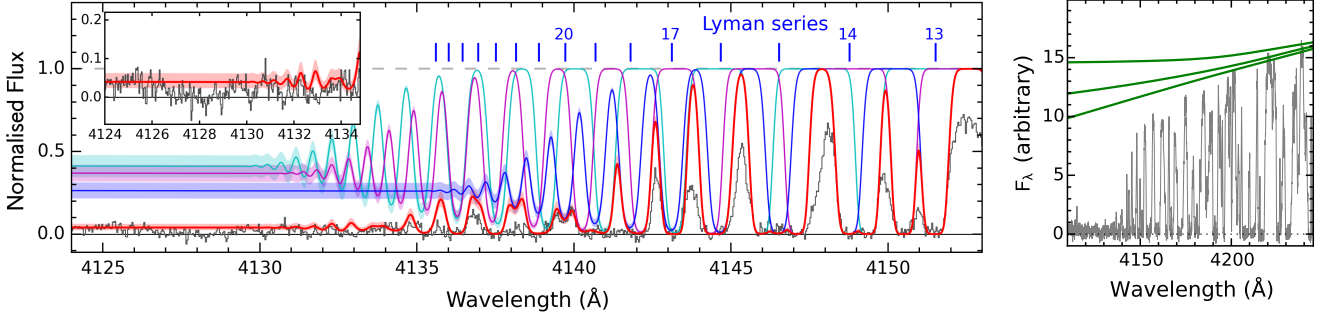


Figure 1. *Left:* Lyman limit for LLS1249 in the spectrum of SDSS J124957.23–015928.8. The quasar spectrum divided by the continuum level is shown in black. Cyan, magenta and blue lines show our model for the three absorption components comprising LLS1249, and red shows the combined absorption model. These components reproduce both the higher order Lyman series absorption at 4134–4152 Å, marked by ticks for component 3 (blue), and the drop in flux at the Lyman limit below 4131 Å. Shading shows 2σ errors on N_{HI} . *Right:* The un-normalised UVES spectrum and the best (middle), highest (top) and lowest (bottom) continuum levels we adopt over the Lyman limit. We estimate the systematic error in N_{HI} associated with continuum estimation as half the difference between N_{HI} values found using the highest and lowest continua, and add this in quadrature to the statistical errors from our Voigt profile fits. The continua over the entire spectrum and for metal transitions of interest are shown in the online supplemental material in Fig. S1–S7.

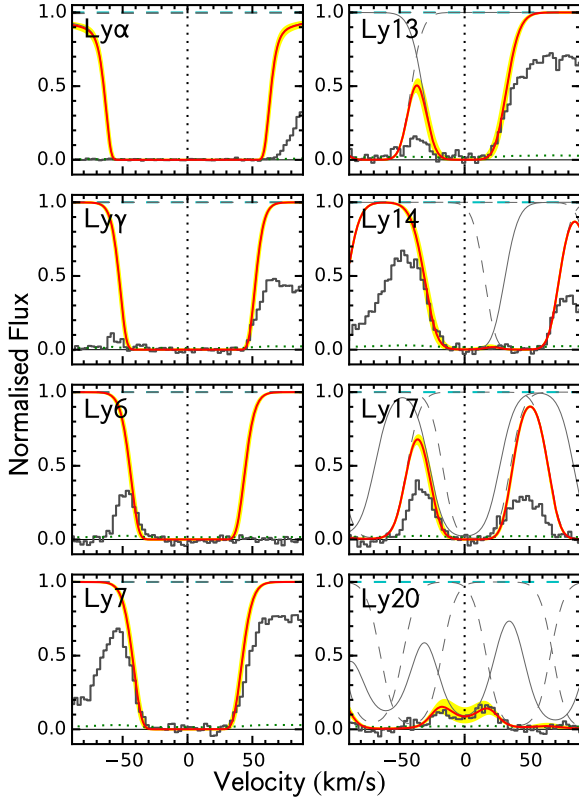


Figure 2. Lyman series for H I component 3. The black histogram shows the quasar spectrum divided by the continuum, and yellow shows the 3σ errors. Absorption from component 3 is shown as a thin solid line, and dashed lines are absorption from the two other components. The thicker red curve shows the combined absorption for all three components, and the dotted line near zero flux is the 1σ uncertainty in the flux. Zero velocity is at the redshift of component 3, $z = 3.530073$. The column density, redshift and b parameter for this component are well determined by multiple Lyman series transitions.

able slope for the incident radiation field, α_{UV} (Crighton et al. 2015). In brief, a single phase, constant density cloud is assumed, illuminated by the UV background radiation from HM12. The CLOUDY code (Ferland et al. 2013, v13.03)

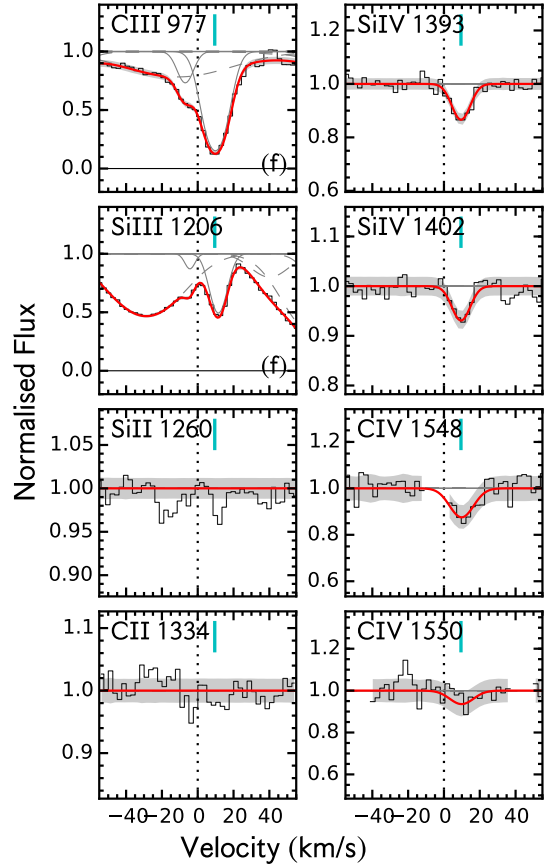


Figure 3. Metal transitions for component 3, where we measure the metallicity and carbon-to-silicon ratio. The cyan vertical ticks show metals from component 3. Grey shaded regions show the 1σ errors in the flux and the red line shows the combined Voigt profile fits. ‘(f)’ means the transition is inside the Ly α forest, and is blended with unrelated H I lines which are shown by dashed profiles. The zero velocity is the H I component redshift. Note the y limits change across different subpanels.

is then used to create a grid of photoionization models with predicted column densities to compare to the observed values listed in Table 2. Our grids cover a range $-4.6 < \log n_{\text{HI}}/\text{cm}^{-3} < -1.0$ (corresponding to $-4.2 < \log U < -0.6$),

$-2.5 < \alpha_{UV} < 1.5$ and $15.5 < \log N_{\text{HI}}/\text{cm}^{-2} < 18.5$. Marginalizing over uncertainties in N_{HI} , the radiation slope, and U we find a 68% range $Z/Z_{\odot} = 10^{-3.41 \pm 0.26}$, and a 95% range $10^{-3.82} < Z/Z_{\odot} < 10^{-2.84}$.

Fig. 4 shows the parameters we derive for component 3. The photoionization models imply a gas temperature $10^{4.35 \pm 0.05}$ K, consistent with the maximum temperature allowed by the H I and metal line widths, and $N_{\text{H}} = 10^{19.8} - 10^{20.8} \text{ cm}^{-2}$ (95% confidence interval). The models favour an ionizing spectrum harder than that in HM12. If no constraint is placed on α_{UV} , the models prefer very hard spectra ($\alpha_{UV} > 1$) which are incompatible with the observed H I and He II photoionization rates (McQuinn & Worseck 2014). Crighton et al. (2015) showed this to be the case at $z = 2.5$, but it should also be true at the redshift of LLS1249, $z = 3.5$, particularly given the quasar space density drops by a factor of 2–3 from $z = 2.5$ to 3.5, which should result in an even softer spectrum at the higher redshift. Therefore we applied a Gaussian prior on α_{UV} with $\sigma = 0.5$ centred on 0. This provides a satisfactory fit to the column densities, while still matching the He II observational constraints. If we require the slope to match the HM12 spectrum precisely (i.e. $\alpha_{UV} = 0$) this results in an even lower metallicity.

Motivated by the small velocity shifts between the H I and metals, described in the following section, we also explore a two component photoionization model in which the metals are not associated with the bulk of the H I. To test this scenario, we ran further ionization models, splitting component 3 into two phases which we allow to have different U . We assume that all of the metal lines are produced in one phase, and require that the amount of H I in this phase is less than the N_{HI} measured for the whole component. This leads to a solution where the metals are produced by a sub-component with $N_{\text{HI}} < 10^{16} \text{ cm}^{-2}$, $U \sim 10^{-2.3}$ and metallicity ~ 0.01 solar. In this case most of the H I would be associated with a second phase that does not have detectable metals. Without any metals detected we are unable to derive a U value, but using the upper limits on metals from the spectrum, and assuming $U > 10^{-3}$ (Fumagalli et al. 2011), we find an upper limit on the metallicity of $Z/Z_{\odot} < 10^{-3.8}$. Therefore this two phase scenario sees a pocket of enriched gas embedded in a surrounding pristine cloud. If this two phase model is correct, our interpretation of the absorbing cloud is unchanged. Indeed, this is entirely consistent with the two scenarios we consider in the next section, which both involve a pristine gas cloud polluted by smaller clumps of more metal-enriched gas.

Finally, we checked that the metallicity of LLS1249 does not depend strongly on the uncertainty in our measured N_{HI} . If we assume an uncertainty in N_{HI} for component 3 of 0.2 dex, more than six times larger than our estimated error in Table 1, the resulting metallicity is $10^{-3.38 \pm 0.26}$, close to our best estimate of $10^{-3.41 \pm 0.26}$.

4 DISCUSSION

Fig. 5 shows our result in comparison to previous metallicity measurements in gas clouds. The metallicity of the diffuse gas ($n_{\text{H}} \sim 10^{-4} \text{ cm}^{-3}$, close to the cosmic mean density) in the intergalactic medium is estimated at $\sim 10^{-3.5}$ solar by statistical analyses of many weak absorption lines

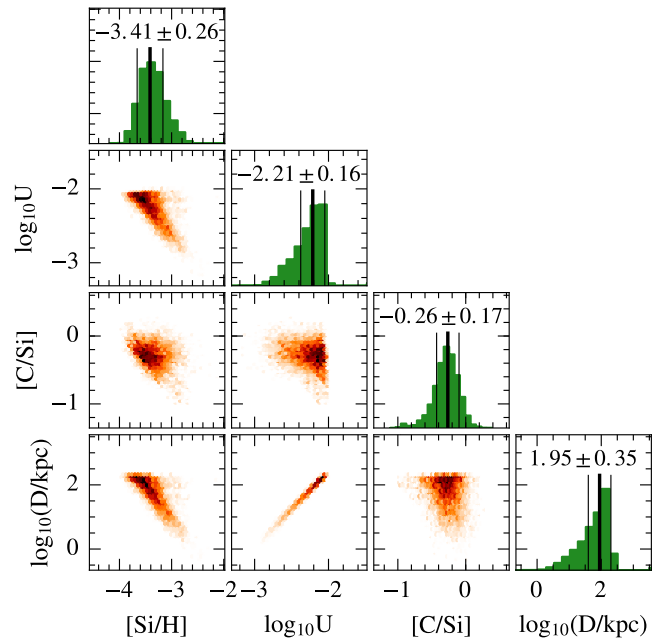


Figure 4. Photoionization model parameters for component 3, where we measure the metallicity and carbon-to-silicon ratio. Panels show the MCMC samples plotted as a function of parameter pairs taken from U , \log_{10} of the metallicity relative to solar $[\text{Si}/\text{H}]$, \log_{10} of the carbon-to-silicon ratio relative to solar $[\text{C}/\text{Si}]$, and the cloud size D . All parameters have flat priors apart from the cloud size, which was required to be $< 200 \text{ kpc}$, and the radiation slope α_{UV} , as described in the text.

(Schaye et al. 2003; Simcoe 2011). Two Lyman limit systems have been discovered without any detectable metals, giving upper limits of $Z/Z_{\odot} < 10^{-4.2}$ and $Z/Z_{\odot} < 10^{-3.8}$ (Fumagalli et al. 2011). When metals have been detected in individual LLS, which we loosely define here as having $10^{17} \text{ cm}^{-2} < N_{\text{HI}} < 10^{20.3} \text{ cm}^{-2}$, they are found at a level $Z/Z_{\odot} > 10^{-3}$ (we show results from the recent compilation by Fumagalli et al. 2015, which includes most known low metallicity LLS, see also Cooper et al. 2015). Recent large samples of metallicity measurements in damped Ly α systems (with $N_{\text{HI}} > 10^{20.3} \text{ cm}^{-2}$) have also not detected metallicities lower than $10^{-3} Z_{\odot}$ (Rafelski et al. 2012; Jorgenson et al. 2013), even in targeted searches for metal-poor systems (Cooke et al. 2011). The metallicity of LLS1249 is thus significantly below those measured in previous strong absorption systems with detectable metals.

The photoionization models imply a carbon-to-silicon ratio $10^{-0.26 \pm 0.17}$ solar for LLS1249. This ratio, together with the overall very low metallicity, suggests two possible origins for the absorbing cloud. The first is enrichment of a pristine cloud by the earliest star formation events in the universe. In this scenario an overdense, pristine region of the early universe collapses to produce PopIII stars, and the death of these first stars curtails further accretion by releasing energy larger than the binding energy of the proto-galaxy. The pristine gas surrounding the proto-galaxy, now polluted with PopIII remnants and unable to collapse further to form new stars, expands with the Hubble flow, producing the absorption we see. Supernovae from higher mass PopIII stars are able to eject their metals to a large distance from the halo, consistent with this scenario (Cooke & Madau 2014). The

yields for these high-mass supernovae predict a carbon-to-silicon ratio consistent with that measured in LLS1249.

Components 1 and 2 in LLS1249 do not have sufficient metal transitions to robustly determine U values, but both do show C III absorption. Assuming the U for these components is similar to component 3 implies they have a similarly low metallicity. Interestingly, for all three components the metal absorption is offset from the velocity of hydrogen by 6–10 km s⁻¹ (Fig. 3 and online supplemental Fig. S8). These shifts are consistent across the UVES and HIRES spectra, taken on different telescopes and with wavelength calibrations calculated by different software. Therefore they are unlikely to be caused by wavelength calibration uncertainties. The bulk of the metals thus have a slightly different velocity structure to the H I, implying they are not well mixed throughout the cloud. Mixing timescales from diffusion and turbulence can be several billions of years (Crighton et al., in preparation), so an inhomogeneous metal distribution is consistent with a Pop III enrichment scenario. The offsets in every component have a similar magnitude and direction, suggesting that a single enrichment event may have been responsible for polluting the H I gas. Assuming a spherical cloud and the densities inferred from photoionization modelling, the minimum mass for the gas producing component 3 is $10^8 M_{\odot}$, which implies a metal mass greater than $10^{-3.4} \times 0.014 \times 10^8 \approx 500 M_{\odot}$. This is significantly more than the metal yield of a single pair-instability supernova, $\lesssim 100 M_{\odot}$ (Heger & Woosley 2002). Therefore if LLS1249 was enriched by a single event it was likely a starburst consisting of at least several supernovae, and not by an individual star. The recent reported observation of a Pop III starburst at $z = 6.6$ may represent such an event (Sobral et al. 2015).

Alternatively, the gas may have been enriched by recent star formation at $z \lesssim 4$. In this scenario pristine gas in either a cold accretion stream (Dekel et al. 2009) or low-mass halo (Cen & Riquelme 2008) is polluted by Population II star formation from a nearby galaxy. We consider a cold stream to be unlikely, however, because they are expected to have a characteristic size of a few kpc and our photoionization models favour much larger cloud sizes (> 6 kpc at 95% confidence). The cloud is also unlikely to be in a low-mass halo, because the velocity width of LLS1249 is > 400 km s⁻¹, more than seven times larger than the virial velocity of a halo with mass $10^{10} M_{\odot}$ at $z = 3.5$. The cloud may be illuminated by ionizing radiation from a quasar, which would be consistent with the hard ionizing spectrum the photoionization models prefer. If this ionizing radiation is much stronger than the integrated UV background we assume, this would also imply higher cloud densities and thus smaller cloud sizes, possibly even consistent with a cold-accretion stream. It would be surprising, however, to find such metal-poor gas in the vicinity of a quasar, which are usually in dense environments (Shen et al. 2007).

New observations of extremely metal-poor absorption systems (e.g. Cooper et al. 2015) will help to clarify the origin of metals in these systems. LLS with higher column densities ($N_{\text{H I}} = 10^{18-20}$ cm⁻²) may be discovered which, even at these low metallicities, show absorption from aluminium, oxygen and nitrogen, in addition to carbon and silicon. The O/Si abundance ratio in particular is sensitive to the assumed Pop III initial mass function (Kulkarni et al. 2013),

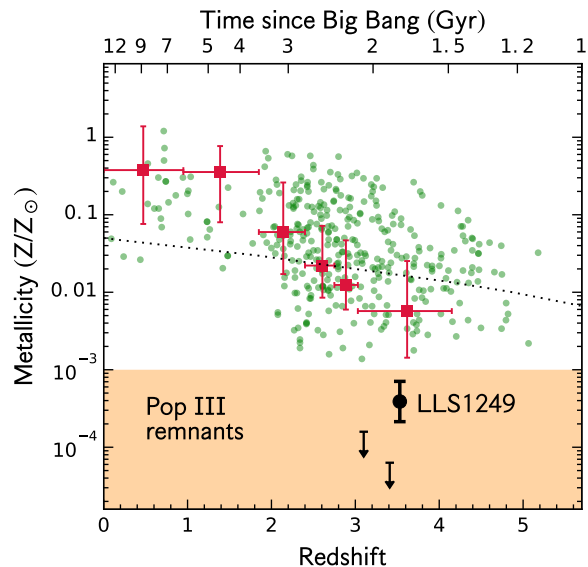


Figure 5. The metallicity of LLS1249 compared to other measurements of diffuse gas metallicities. Green dots show representative metallicities for the predominantly neutral damped Lyman- α systems (see text); their typical uncertainties are 0.2 dex. Red squares show metallicities for a compilation of the more highly ionized Lyman limit systems (Fumagalli et al. 2015). Vertical errors on the squares show the 25–75% range in the sample metallicity probability distribution. Upper limits from Fumagalli et al. (2011) are shown as arrows. The large dot with error bars shows our measurement in LLS1249 and its 1σ uncertainty. The dotted line shows an analytic model for the cosmological evolution of gas metallicity (Hernquist & Springel 2003). The shaded region shows predictions for gas metallicities resulting from Pop III star formation events (Wise & Abel 2008; Wise et al. 2012).

and will enable a more detailed comparison to be made with models of pristine gas enrichment.

ACKNOWLEDGEMENTS

NHMC and MTM thank the Australian Research Council for *Discovery Project* grant DP130100568 which supported this work. Our analysis made use of ASTROPY (Astropy Collaboration et al. 2013), UVES_POPLER (http://astronomy.swin.edu.au/~mmurphy/UVES_popler), HIRESREDUX (<http://www.ucoick.org/~xavier/HIRESredux>), VPFIT (<http://www.ast.cam.ac.uk/~rfc/vpfit.html>), and MATPLOTLIB (Hunter 2007). This work used archived data taken at the ESO La Silla Paranal Observatory for program 075.A–0464 (P.I. Kim) and at the W. M. Keck Observatory for program U157hb (P.I. Prochaska). The authors wish to acknowledge the significant cultural role that the summit of Maunakea has always had within the indigenous Hawaiian community. We are most fortunate to have the opportunity to conduct observations from this mountain.

REFERENCES

- Astropy Collaboration et al., 2013, *A&A*, **558**, A33
- Bagdonaite J., Murphy M. T., Kaper L., Ubachs W., 2012, *MNRAS*, **421**, 419
- Becker G. D., Bolton J. S., 2013, *MNRAS*, **436**, 1023
- Bromm V., 2013, *Reports on Progress in Physics*, **76**, 112901
- Cen R., Riquelme M. A., 2008, *ApJ*, **674**, 644

- Ciardi B., Ferrara A., 2005, *Space Sci. Rev.*, **116**, 625
 Cooke R. J., Madau P., 2014, *ApJ*, **791**, 116
 Cooke R., Pettini M., Steidel C. C., Rudie G. C., Nissen P. E., 2011, *MNRAS*, **417**, 1534
 Cooper T. J., Simcoe R. A., Cooksey K. L., O’Meara J. M., Torrey P., 2015, preprint, ([arXiv:1505.06210](https://arxiv.org/abs/1505.06210))
 Crighton N. H. M., Hennawi J. F., Simcoe R. A., Cooksey K. L., Murphy M. T., Fumagalli M., Prochaska J. X., Shanks T., 2015, *MNRAS*, **446**, 18
 D’Odorico V., Petitjean P., 2001, *A&A*, **370**, 729
 Dekel A., et al., 2009, *Nature*, **457**, 451
 Ferland G. J., et al., 2013, *Rev. Mex. Astron. Astrofis.*, **49**, 137
 Fumagalli M., O’Meara J. M., Prochaska J. X., 2011, *Science*, **334**, 1245
 Fumagalli M., O’Meara J. M., Prochaska J. X., 2015, Submitted to MNRAS
 Haardt F., Madau P., 2012, *ApJ*, **746**, 125
 Heger A., Woosley S. E., 2002, *ApJ*, **567**, 532
 Heger A., Woosley S. E., 2010, *ApJ*, **724**, 341
 Hernquist L., Springel V., 2003, *MNRAS*, **341**, 1253
 Hunter J. D., 2007, *Computing in Science and Engineering*, **9**, 90
 Jorgenson R. A., Murphy M. T., Thompson R., 2013, *MNRAS*, **435**, 482
 Kulkarni G., Rollinde E., Hennawi J. F., Vangioni E., 2013, *ApJ*, **772**, 93
 Lehner N., O’Meara J. M., Fox A. J., Howk J. C., Prochaska J. X., Burns V., Armstrong A. A., 2014, *ApJ*, **788**, 119
 Levshakov S. A., Agafonova I. I., Centurión M., Molaro P., 2003, *A&A*, **397**, 851
 McQuinn M., Worseck G., 2014, *MNRAS*, **440**, 2406
 O’Meara J. M., et al., 2015, preprint, ([arXiv:1505.03529](https://arxiv.org/abs/1505.03529))
 Planck Collaboration et al., 2015, preprint, ([arXiv:1502.01589](https://arxiv.org/abs/1502.01589))
 Prochaska J. X., Burles S. M., 1999, *AJ*, **117**, 1957
 Rafelski M., Wolfe A. M., Prochaska J. X., Neeleman M., Mendez A. J., 2012, *ApJ*, **755**, 89
 Schaye J., Aguirre A., Kim T.-S., Theuns T., Rauch M., Sargent W. L. W., 2003, *ApJ*, **596**, 768
 Schneider D. P., et al., 2003, *AJ*, **126**, 2579
 Shen Y., et al., 2007, *AJ*, **133**, 2222
 Simcoe R. A., 2011, *ApJ*, **738**, 159
 Simcoe R. A., Sargent W. L. W., Rauch M., 2002, *ApJ*, **578**, 737
 Sobral D., Matthee J., Darvish B., Schaerer D., Mobasher B., Röttgering H., Santos S., Hemmati S., 2015, preprint, ([arXiv:1504.01734](https://arxiv.org/abs/1504.01734))
 Wise J. H., Abel T., 2008, *ApJ*, **685**, 40
 Wise J. H., Turk M. J., Norman M. L., Abel T., 2012, *ApJ*, **745**, 50
 Yoshida N., Bromm V., Hernquist L., 2004, *ApJ*, **605**, 579

Supplementary online material

This paper has been typeset from a $\text{\TeX}/\text{\LaTeX}$ file prepared by the author.

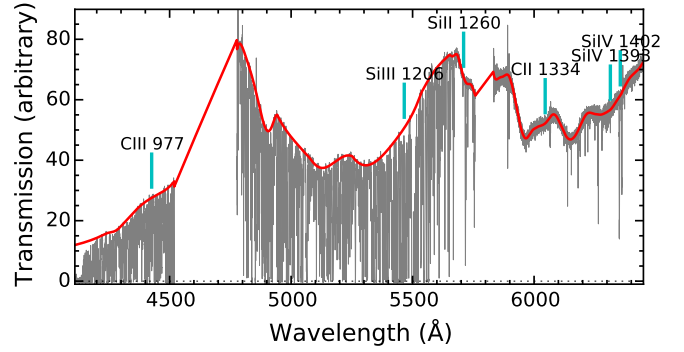


Figure S1. The UVES spectrum used to measure H I and metal line parameters. The adopted continuum is shown in red, and ticks show the positions of important metal transitions for component 3 in LLS1249. The QSO Ly α emission line is near 5650 Å. The spectrum is not flux-calibrated, and the scaling of the transmission is arbitrary. The large gaps at 4500–4800 Å and 5750–5850 Å are regions of the spectrum not covered by the UVES observations.

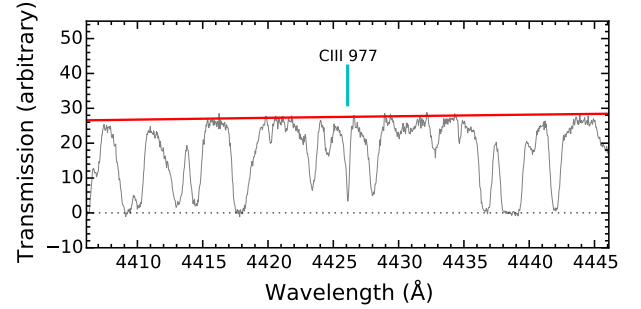


Figure S2. The continuum around C III 977 for component 3.

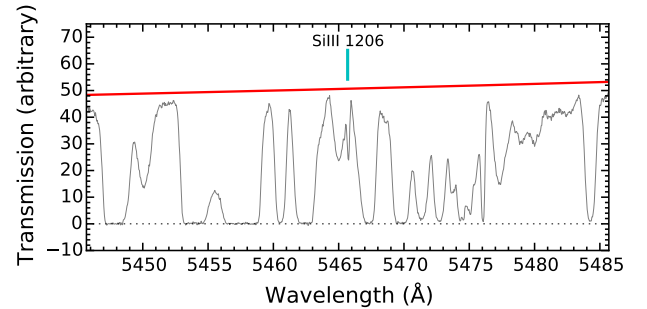


Figure S3. The continuum around Si III 1206 for component 3.

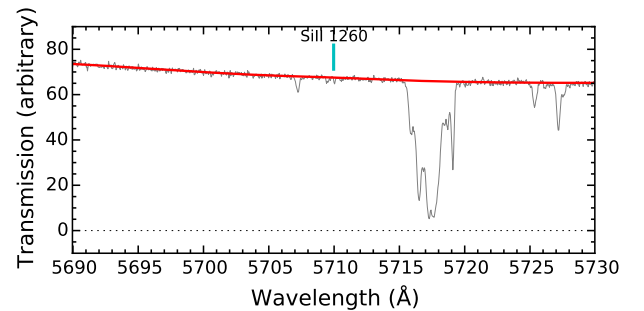


Figure S4. The continuum around Si II 1260 for component 3.

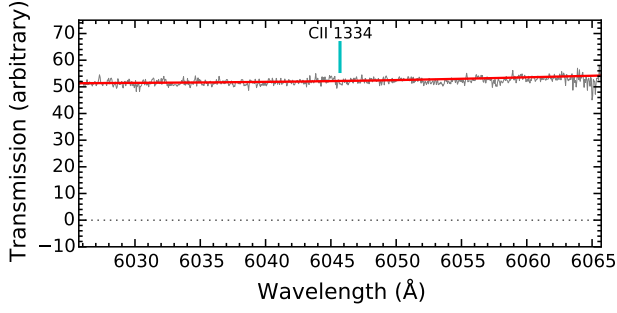


Figure S5. The continuum around C II 1334 for component 3.

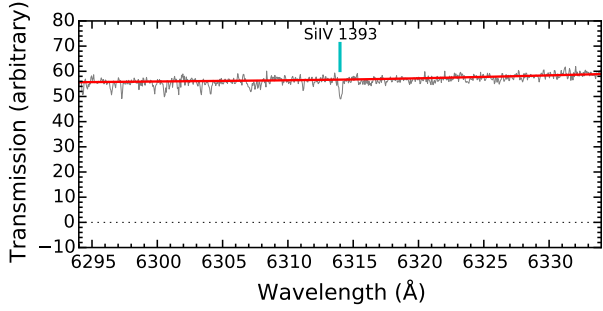


Figure S6. The continuum around Si IV 1393 for component 3.

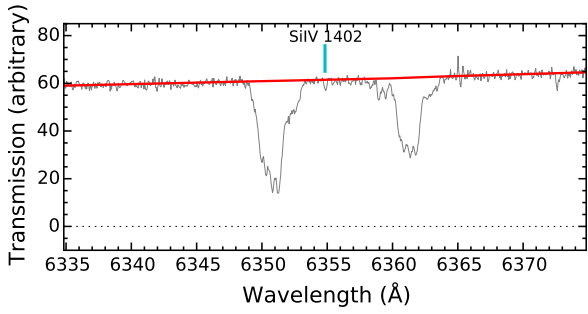


Figure S7. The continuum around Si IV 1402 for component 3.

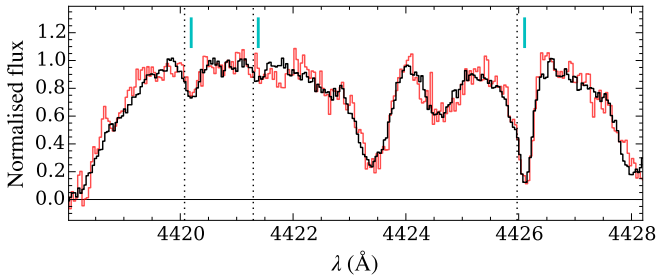


Figure S8. The UVES (black) and HIRES (red) spectra of the C III 977 transition for all three components in LLS1249. Both spectra show a shift between the redshift of the H I components, shown by dotted lines, and the metal line redshifts, shown by cyan ticks.